Shape-Anisotropy Driven Symmetry Transformations in Nanocrystal Superlattice Polymorphs

Kaifu Bian,[†,⊥] Joshua J. Choi,[‡,⊥] Ananth Kaushik,[†] Paulette Clancy,[†] Detlef-M. Smilgies,[§] and Tobias Hanrath[†,*]

[†]School of Chemical and Biomolecular Engineering, [‡]School of Applied and Engineering Physics, and [§]Cornell High Energy Synchrotron Source (CHESS), Cornell University, Ithaca, New York 14853, United States. [⊥] These authors contributed equally to this work.

Interactions between nanocrystals (NCs) solubilized by surface-bound organic ligands have often been, to a first approximation, described by a spherically symmetric interaction potential: The softness of the ligand shell can be parametrized by the ratio (χ) of the ligand length (l) to the particle radius (r) (*i.e.*, $\chi = l/r$).[1,2] Colloids and relatively large diameter NCs up to $\chi \approx 0.7$ interact as hard spheres and form close-packed assemblies with fcc symmetry. In contrast, softer NCs, beyond $\chi > 0.7$, favor more open structures in which the flexible ligands occupy interstitial space in the bcc superlattice.[1,2] On the basis of this model, the oleic acid-passivated PbSe and PbS NCs with $\chi = 0.5-0.6$ investigated in this work would be expected to form fcc superlattices. However, the basic hard/soft sphere model is inadequate. We will show that identical NCs can be assembled into NCSLs with predefined symmetries by adjusting the nature of the ligand–solvent interactions.

Instead of the expected fcc ordering, the GISAXS pattern of the PbS NCSL in Figure 1 reveals a noncubic symmetry that can be uniquely indexed to the reflections of a bct NCSL with $a = b = 9.8$ nm and $c = 12.4$ nm. The $(110)_{SL}$ plane of this NCSL is oriented parallel to the plane of the substrate. The bct symmetry can be viewed as an intermediate between the fcc ($c/a = \sqrt{2}$) and bcc ($c/a = 1$) lattice symmetry along the Bain deformation path (see Figure 1c).[3]

Bain deformations occur in various atomic crystals and block copolymers and remain a subject of ongoing investigation in condensed and soft matter physics.[4–8] It is important to note that the tetragonal distortion of the bct NCSLs occurs along the $[001]_{SL}$ directions, which are neither parallel nor perpendicular to the plane of the substrate.

ABSTRACT Despite intense research efforts by research groups worldwide, the potential of self-assembled nanocrystal superlattices (NCSLs) has not been realized due to an incomplete understanding of the fundamental molecular interactions governing the self-assembly process. Because NCSLs reside naturally at length-scales between atomic crystals and colloidal assemblies, synthetic control over the properties of constituent nanocrystal (NC) building blocks and their coupling in ordered assemblies is expected to yield a new class of materials with remarkable optical, electronic, and vibrational characteristics. Progress toward the formation of suitable test structures and subsequent development of NCSL-based technologies has been held back by the limited control over superlattice spacing and symmetry. Here we show that NCSL symmetry *can* be controlled by manipulating molecular interactions between ligands bound to the NC surface and the surrounding solvent. Specifically, we demonstrate solvent vapor-mediated NCSL symmetry transformations that are driven by the orientational ordering of NCs within the lattice. The assembly of various superlattice polymorphs, including face-centered cubic (fcc), body-centered cubic (bcc), and body-centered tetragonal (bct) structures, is studied in real time using *in situ* grazing incidence small-angle X-ray scattering (GISAXS) under controlled solvent vapor exposure. This approach provides quantitative insights into the molecular level physics that controls solvent–ligand interactions and assembly of NCSLs. Computer simulations based on all-atom molecular dynamics techniques confirm several key insights gained from experiment.

KEYWORDS: nanocrystals · Bain transformation · self-assembly · vapor annealing · *in situ* characterization · grazing-incidence small-angle X-ray scattering

Therefore, the deformation is not the result of macroscopic film shrinkage or lateral stresses during drying, but instead reflects the intrinsic symmetry of the NCSL. Importantly, the grazing-incidence wide-angle X-ray scattering (GIWAXS) pattern from individual NCs reveals a high degree of orientational coherence of NCs in their lattice sites. Specifically, the simultaneous small- and wide- angle X-ray scattering data illustrate the coaxial alignment of $(110)_{SL}$ and $(110)_{NC}$ planes of the superlattice (SL) and nanocrystal (NC) lattices, respectively.

The hypothesis tested and confirmed in this paper is that the orientational ordering of NCs drives the coherent distortion superlattice symmetry. We note that the Archimedean

(a)

(b)

(c)

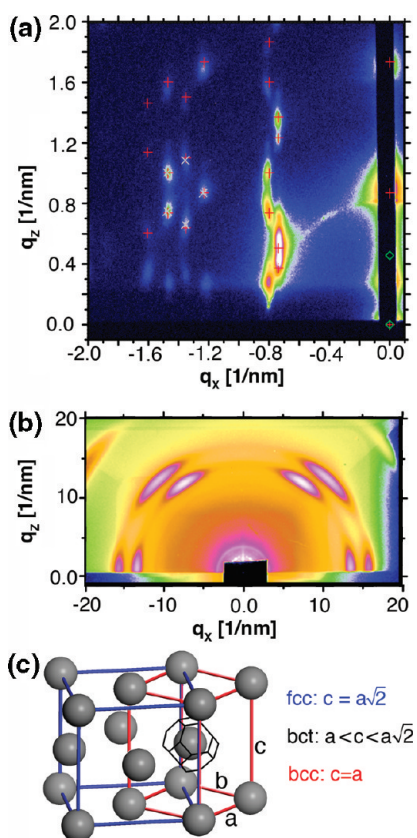

fcc: $c = a\sqrt{2}$

bct: $a < c < a\sqrt{2}$

bcc: $c = a$

Figure 1. Tetragonally distorted NCSL (a) GISAXS pattern of a bct superlattice ($a = b = 9.8$ nm, $c = 12.4$ nm) with $(110)_{SL}$ planes parallel to the substrate and 7% shrinkage (s) in the vertical direction; (b) corresponding GIWAXS patterns illustrating coaxial alignment of $[110]_{NC}$ axis of NCs in their superlattice sites; (c) model of the fcc and bcc unit cells related through the Bain deformation. The experimental setup for the GISAXS measurements is shown in the Supporting Information.

cuboctahedron, a special member of this family of shapes which produces a perfect space filling, has just the observed structural property. In our NC structure the ligand shell between NC cores can accommodate deviations from the perfect shape, and thus cuboctahedra close to the Archimedean one show a natural tendency to assume such a dense bcc packing of nonspherical particles. Hence despite the fact that cuboctahedra are almost spherical, the proximity of the densely packed phase seems to drive the NCSL toward the bcc structure.

The broken symmetry underlying the formation of a nonclose-packed bct NCSLs with translational and orientational order illustrated in Figure 1 is remarkable and leads to a number of intriguing questions. In particular, what is the driving force behind this symmetry distortion and the NC orientational ordering? And how can we tailor the driving force to control the assembly of NCSLs with predefined symmetries?

RESULTS AND DISCUSSION

To understand the fundamental origin of the tetragonal NCSL distortion and its relation to the symmetry of

the interaction potential, we considered two alternative hypotheses: (1) electrostatic interactions resulting from dipole–dipole coupling of proximate NCs and (2) forces based on anisotropic interactions between the surface-bound ligand chains.[9]

The hypothesis that dipole–dipole interactions form the driving force behind the coherent NCSL distortion was inspired by analogies to similar effects in atomic crystals. The Jahn–Teller effect and martensitic phase transitions are the prominent examples of electronic interactions leading to lattice structure transformations in atomic systems.[3,10−13] Since NCSLs can be regarded as artificial crystals, we conjectured that similar symmetry distortions may arise from the dipole–dipole interactions of neighboring NCs. The dipoles are believed to arise from an uneven distribution of Pb- and Se-terminated $\{111\}_{NC}$ facets of individual NCs[14] with cuboctahedron shapes or charged surface states.[15] Dipole pair interactions, whose strength was recently estimated to be in the range of $8-10\ k_B T$,[16] have been attributed as the driving force in the formation of highly anisotropic nanostructures, via oriented attachment,[14,17] and the assembly of NC films with nonclose-packed, simple hexagonal, symmetry.[18]

The uniformity of the NC dipoles is a crucial factor in understanding their possible role in coherent NCSL distortions. Cho et al. have analyzed possible NC dipoles resulting from an even (i.e., 4:4) distribution of Pb- and Se-terminated $\{111\}_{NC}$ facets.[14] Recent theoretical and experimental work by Fang et al. suggested that the $\{111\}_{NC}$ facets are composed of ribbons of alternating polarity that are stabilized in the presence of surface bound ligands and in their absence transform to ribbon-like Pb or Se nanodomains.[19] Other reports indicated that the composition of lead salt NCs varies significantly depending on synthesis parameters and is, in most cases, characterized by an excess of lead.[20,21] We determined the more general relationship between Pb- and chalcogen-terminated $\{111\}_{NC}$ facets and found 163 nonequivalent configurations resulting in a broad distribution of dipole strength and direction (see Supporting Information Figure S1). The inhomogeneity of the dipole distribution is inconsistent with the requirements for a coherent NCSL distortion observed in our experiments and provides a strong indication against a major role of dipole interactions in the coherent distortion of NCSLs.

To prove this interpretation and to differentiate between dipolar and ligand–ligand interactions, we devised an experiment that exploits differences in the potential–distance relationship of the two interactions. The ligand–ligand interactions fall off over shorter distances comparable to the length of the ligand molecule; electrostatic interactions between NC facets and related permanent dipoles and multipoles are significant over much larger ranges.[9] A common approach to tune interparticle spacing in NC assemblies is
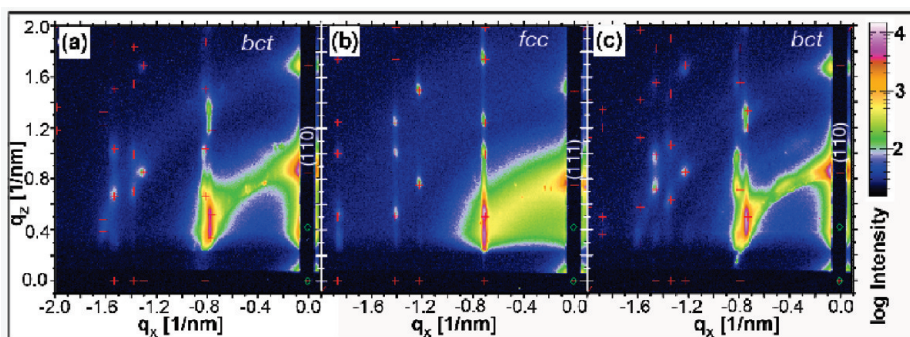
Figure 2. Reversible tetragonal-cubic phase transition: (a) dry bct PbSe NCSL ($a = b = 9.7$ nm, $c = 12.1$ nm, $s = 2.5\%$); (b) fcc superlattice in the presence of 75% saturated octane vapor ($c = \sqrt{2}a = 14.5$ nm, $s = 0\%$); (c) rapidly dried bct superlattice ($a = b = 10.3$ nm, $c = 12.1$ nm, $s = 6\%$).

to tailor the interface chemistry, for example, through the substitution of variable chain length ligands; this approach has provided critical insights into the complex relationship of soft ligands/hard core interactions.[1,2,9] Unfortunately, the ligand exchange inevitably introduces a number of additional complications including changes in surface chemistry (*i.e.*, dipole), solubility, and NC morphology.[20−22] To avoid these perturbations, we pursued an alternative approach that preserves the NC surface chemistry and enables *reversible* and *continuous* tuning of interparticle spacing through solvent vapor processing. We have previously demonstrated this approach as a powerful technique to improve the long-range ordering of NCSLs.[23] Here, we integrate solvent vapor processing with *in situ* GISAXS analysis to study solvent vapor-mediated changes in NCSL structure in real time.

The starting point for the *in situ* measurements was a PbSe NC film, drop-cast under ambient conditions from a 0.05 mg/mL colloidal NC suspension in hexane. We investigated both PbS and PbSe NCSL and found that the trends in NCSL symmetry were independent of chalcogenide composition in the NC core. The corresponding GISAXS pattern (Figure 2a) of the PbSe NCSL can be indexed to a bct structure (space group: *I*4/*mmm*, No. 139) with $a = b = 9.7$ nm, $c = 12.1$ nm. The anisotropic broadening of the Bragg reflection is due to the fact that the lateral NCSL grain exceeds the film thickness. Using Scherrer's formula,[24] we determined the vertical and horizontal grain size to be 48 and 154 nm, respectively, by analyzing the radial widths of various reflections and extrapolating to the vertical and horizontal intrinsic width of the $(113)_{SL}$, $(-131)_{SL}$, and $(22-2)_{SL}$ NCSL reflections (see Supporting Information section 4).

Next, we exposed the NCSL to gradually increasing concentrations of octane vapor and monitored changes in the NCSL symmetry. We observed a tetragonal-to-cubic (bct-to-fcc) symmetry transformation after exposing the NC film to a subsaturated (∼0.60 mol/m^3) octane vapor atmosphere for approximately 4 min. The corresponding GISAXS pattern (Figure 2b) reveals a fcc (space group $Fm\bar{3}m$, No. 225) (*i.e.*,

undistorted) NCSL with $c = \sqrt{2}a = 14.5$ nm. For consistency, we will describe lattice constants of fcc, bct, and bcc crystals in terms of the general unit cell illustrated in Figure 1c. The 34% increase in unit cell volume relative to the initial bct NCSL can be attributed to solvent swelling and capillary condensation of vapor in the interstitial spaces of the NC film;[25] the low-q scattering is due to the NC suspension in a disordered, liquid state that eventually crystallizes.

To quantitatively analyze the NCSL spacing in the context of the spatial arrangement of the NC cores and the surface-bound ligands, we define the interparticle spacing, δ, as the distance between NC surfaces along the close-packed direction, that is, the space available to ligands and possibly solvent molecules. We determined the average NC diameter ($d_{NC} = 6.1$ nm) from a statistical analysis of transmission electron microscopy (TEM) images. In the case of the bct NCSL in Figure 2a, the spacing along the close-packed $[111]_{SL}$ direction of the bct lattice is $\delta = (2a^2 + c^2)^{1/2}/2 - d_{NC} = 3.0$ nm; this spacing is less than twice the length of the oleic acid ligand ($L_{OA} \approx$ 1.8 nm) and illustrates that there is partial overlap of the ligands bound to the surfaces of adjacent NC cores.[22]

On the other hand, analysis on the swollen fcc NCSL (Figure 2b) shows that the interparticle separation along the close-packed $\langle 110 \rangle_{SL}$ direction of δ is 4.1 nm, or approximately 2.3 L_{OA}; this comparison illustrates that the ligands of proximate NCs in the swollen superlattice do not overlap. We can therefore conclude that the tetragonal NCSL distortion that occurs only in situations where ligands of neighboring NCs overlap (*i.e.*, interparticle separation $\delta < 2L_{OA}$.) underscores the critical role of molecular interactions. Alternatively, if the longer range NC dipole−dipole interactions were the cause of the tetragonal NCSL distortion, then even the swollen NCSLs should exhibit bct symmetry. Instead, the bct-to-fcc transition illustrated in Figure 3 provides direct experimental evidence to eliminate the role of dipole interactions.

The cubic-to-tetragonal symmetry transformation is fully reversible. The bct NCSL symmetry can be restored by reducing the octane vapor concentration.
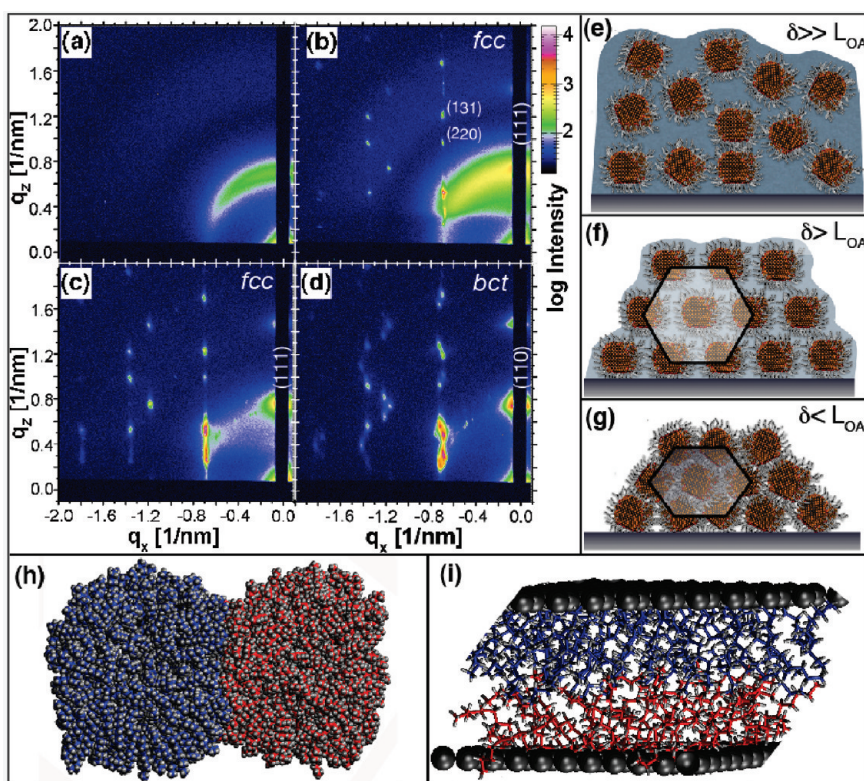
Figure 3. *In-situ* GISAXS patterns of solvent-vapor mediated PbS NCSL symmetry transformations: (a) disordered film in a saturated octane vapor environment (~0.8 mol/m³); (b) initial superlattice nucleation in a subsaturated vapor environment (~40% saturation); (c) fcc NCSL formed by drying the film over the course of 3 h ($c = \sqrt{2}a$ = 13.7 nm); (d) bct NCSL formed by drying the film in the presence of He purge ($a = b$ = 9.8 nm, c = 13.0 nm); (e–g) schematic of the disordered, swollen fcc, and dry bct nanocrystal film. Note, the deformed hexagon illustrates a minor superlattice shrinkage (~4%) in the vertical direction, while more pronounced tetragonal distortions occur along the $[100]_{NC}$ fcc NCSL direction. (h) MD snapshot of two NCs with (i) high resolution snapshot of a MD simulation of ligands between $(111)_{NC}$ facets of proximate NCs.

Figure 2c shows the scattering signature of a bct structure with $a = b$ = 10.3 nm and c = 12.1 nm, which was formed by quickly evaporating the condensed solvent in the presence of a He purge flow. We note that the extent of the tetragonal lattice distortion is sensitive to the solvent evaporation rate as controlled by the He purge flow. The relationship between lattice distortion and solvent evaporation rate controlled by fine-tuning the evaporation conditions may shed new light on kinetic effects of ligand effects during the assembly, while at the same time introducing refined control over the NCSL symmetry.

We turned to *in situ* GISAXS measurements to monitor the assembly dynamics in real time to gain deeper insights into the relationship between solvent evaporation rate, NCSL growth, and symmetry. In the presence of saturated octane vapor, solvent uptake in the NCSL first swells the assembly and ultimately results in completely disordered thin films of the saturated NC suspension (see Figure 3a and integrated intensity profiles in the Supporting Information Figure S5).

We progressively reduced the solvent vapor concentration and monitored the concurrent decrease in interparticle spacing indicated by the scattering profile. This approach allowed us to determine the critical interparticle separation corresponding to the order/disorder transition at the NCSL nucleation. We observed the first signs of NCSL nucleation at octane vapor concentrations corresponding to ~40% saturation (~0.32 mmol/L). The sharp scattering features of the nascent NCSL indicate fcc symmetry with a lattice constant of $c = \sqrt{2}a$ = 15.2 nm and a grain size on the order of 800–1200 nm. The detailed grain size analysis provided in the Supporting Information shows that NCSL grain size of the nascent NCSL is substantially larger than the ~140 nm grains calculated from the GISAXS peak of the final (dry) supercrystal. We attribute this grain size reduction to cracking inherent to drying wet films.[23] The interparticle separation between the 6.4 nm core PbS NCs along the close-packed $[110]_{SL}$ direction of the nascent fcc lattice was δ = 4.3 nm = $2.4L_{OA}$, which significantly exceeds the reach of the ligands; this confirms the lack of ligand overlap, similar to the case of the swollen PbSe NCSL in Figure 2b and shows that solvent molecules take up a significant volume in the initial NCSL. If the NCs are modeled as spheres, the volume packing fraction in the initial NCSL corresponds to approximately 0.6.

We investigated the solvent evaporation rate as an independently adjustable parameter to control the

extent of tetragonal distortion in the resulting NCSL. By tuning the He purge flow rate in the *in situ* cell, we systematically scanned solvent evaporation times ranging from several hours to less than one minute and returned the NC film to the disordered state (Figure 3a, e) in between each run. Slow growth of NCSL, in which the solvent evaporation was controlled over a period of over 3 h, exhibited fcc symmetry with a lattice constant of $c = \sqrt{2}a = 13.7$ nm (Figure 3c). When we accelerated the growth rate by reducing the solvent evaporation time to approx 30 s, we formed a NCSL with bct symmetry and $a = b = 9.8$ nm and $c = 13.0$ nm (Figure 3d). The extent of ligand overlap along the close-packed superlattice direction in both cases is approximately the same, and comparable to the case of PbSe NCSL shown above. At even faster evaporation rates, the resulting NC film exhibited ring-like scattering signatures (similar to the pattern shown in the Supporting Information Figure S7), indicating that the planes of the formed NCSL were not aligned parallel to the underlying substrate.[23] Notably, these kinetic effects are distinct from the crystallization of metastable bcc crystals in atomic systems in which bcc crystals often nucleate first even if fcc phase is more thermodynamically stable.[26]

We further confirmed the relationship between NCSL-symmetry and -growth rate in a series of control experiments in which we tuned the growth rate by adjusting the concentration of NCs in the initial suspension. NCSLs formed from dilute NC suspensions (0.05 mg/mL) in 9:1 v/v hexane/octane, corresponding to slow growth rate formed fcc NCSLs; higher colloidal NC concentrations, in the range of 0.5–5.0 mg/mL yielded NCSLs with bct symmetry (see Supporting Information Figure S7).

Two important concepts emerge from the results of these experiments. First, systematic adjustment of the solvent evaporation rate enables control over the symmetry and spatial coherence of the resulting NCSLs. Second, the symmetry of the self-assembled NCSLs is governed by ligand interactions that are not captured in previous hard sphere/soft shell models. We illustrate how anisotropic ligand coverage on specific NC facets influences NCSL symmetry in a separate publication.[27]

Insights into the detailed molecular-level interactions between surface bound ligands are beyond the capabilities of current experimental approaches and instead rely on computational simulations. Luedtke and Landman have previously demonstrated the advantages of molecular dynamics (MD) simulations of alkyl thiol-passivated gold NCs to show that surface-bound ligands organize into orientationally distinct ligand "bundles" between proximate NCs leading to tetragonal NCSL distortions similar to those observed in our work.[28,29] We performed MD simulations of oleic acid-passivated lead salt NCs to test whether similar ligand bundling is responsible for the aspherical interactions observed in our experiments. Our simulations suggest that oleic acid ligands do not invariably form bundles as in the case of alkyl thiol-passivated Au NCs; instead, they exhibit a complex array of ligand–ligand response to assembly that varies from interpenetration to ligand avoidance. This response depends on factors such as ligand surface coverage density, NC diameter, NC core shape, the rate at which NCs approach during self-assembly, *etc.* in ways consistent with the dendrimer packing computational studies of Li *et al.*[30] Detailed results from these simulations and corresponding GISAXS measurements will be reported in an upcoming publication.

Experimental efforts confirm the MD-derived prediction that bundling is not a prevalent motif; probing the presence of quasi-crystalline ligand bundles using polarized infrared spectroscopy showed no discernible spectroscopic signatures that could be ascribed to bundles (see Supporting Information Figure S9).[31] Moreover, ligand bundles should lead to temperature-dependent interaction potentials governing the self-assembly. While trends between assembly temperature and NCSL symmetry have recently been reported in the case of Ag NCs,[32] our GISAXS experiments at variable temperatures have, to date, not shown such correlations in oleic acid-terminated lead salt NCs.

Although not in the form of ordered bundles, our simulations do show that ligands experience a net attraction along the close-packed direction within the NCSL (see Figure 3h,i), consistent with previous experimental reports of ligand distributions in metal NC monolayer assemblies.[33] Our model shows that the outcome of van der Waals interactions between ligands on neighboring NCs depends on the *rate* at which the interparticle separation is reduced. Under molecular simulation conditions commensurate with slow solvent evaporation (Figure 3c), achieved by bringing the ligands on approaching NCs together "slowly" (at rates of ∼0.2 Å/ps or 0.02 Å/ps) the ligands are able to relax and interdigitate (see Supporting Information section 8). The interaction potential in this scenario remains essentially spherically symmetric throughout. At a faster approach (∼2.5 Å/ps), commensurate with the experimental case of accelerated solvent evaporation (Figure 3d) or higher colloidal NC concentration (see Supporting Information Figure S7), repulsive interactions between the ligands dominate. Unable to interdigitate during their rapid approach, the ligand–ligand repulsions perturb the spherically symmetric interaction potential. This perturbation, together with the limited relaxation time during a fast drying process, pushed and trapped the NCSL system into a tetragonally distorted state which is a metastable configuration (see Supporting Information section 8).

These molecular-level insights into the early stages of NCSL assembly suggest that rational modifications of the relative strength of ligand–ligand and ligand–solvent interactions present an additional degree of freedom to control the structure of the NCSL assembly. To
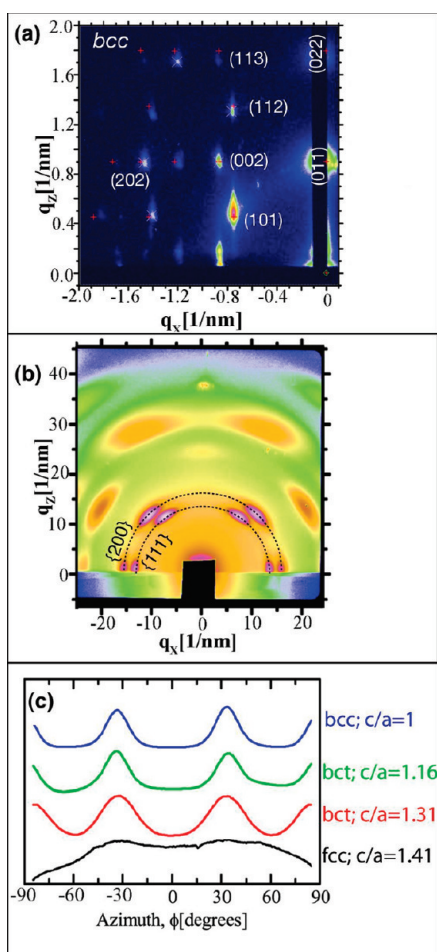
Figure 4. NCSL with bcc symmetry: (a) GISAXS pattern of a (110)$_{SL}$ oriented bcc superlattice ($a = b = c = 11$ nm); (b) corresponding wide-angle scattering pattern illustrating the coaxial [110]$_{NC}$ alignment with the substrate-induced [110]$_{SL}$ normal orientation of the superlattice; (c) orientation distribution function of the (100)$_{NC}$ Bragg planes in NCSLs with bcc, bct, and fcc NCSL symmetry. The plots were obtained by radially integrating the intensity of the (111)$_{NC}$ reflections as a function of detector azimuthal angle (ϕ).

demonstrate this concept, we compared ligand–solvent interactions in the case of the aliphatic chain of the fatty acid ligand solvated by various solvents. Guided by considerations of Flory–Huggins interaction parameters and molecular shapes, we expected aliphatic solvents (e.g., hexane, octane) to solubilize the ligand chain more effectively than the aromatic solvents (e.g., toluene). In other words, in an aromatic solvent, proximate NCs will arrange themselves to maximize ligand–ligand interactions and to avoid the energetically less favorable ligand–solvent interactions.

We tested this conjecture by repeating the *in situ* GISAXS measurements in the presence of toluene vapor and found that toluene mediates the assembly of NCSLs with undistorted bcc symmetry (space group: *Im*3*m*, No. 229). A NCSL with an initial bct symmetry ($a = b = 10.3, c = 12.3$) assembled from hexane suspension was exposed to toluene vapor resulting in a disordered (molten) intermediate state which upon drying recrystallized as an

undistorted bcc NCSLs ($a = 11.0$ nm) (Figure 4a). We note that the interparticle spacing along the close-packed [111] direction of the initial bct and final *b*cc NCSL is approximately the same. Moreover, it is important to point out that NCSLs formed in the presence of toluene vapor exhibit bcc symmetry for a wide range of drying rates. The lack of a relationship between drying rate and superlattice distortion, as was observed in the case of hexane and octane vapor (see Figure 2), suggests that NCSL self-assembly in toluene is dominated by energetic aspects of ligand–ligand interactions.

The failure of the soft sphere model in the case of lead salt NCs with $\chi < 0.7$ suggests that other aspects of the NC interaction need to be considered. An earlier investigation of binary NCSLs by O'Brien and co-workers introduced the idea of "hard spheres with sticky soft shells".[34] Building on their model, we hypothesized that the "stickiness" of the ligand shell is related to the symmetry of the NC core. The relative ligand density on the NCs {111}$_{NC}$ and {100}$_{NC}$ facets is not known and is subject to current computational and experimental investigation in our laboratory. Parallels between the 8-fold coordination of the single-component bcc NCSL and the 8-fold symmetry of {111}$_{NC}$ facets on individual cuboctahedral NCs, which was reported by Fang *et al.* to be an energetically preferred Wulff construction,[19] provides an important clue: In the case of toluene vapor, neighboring ligands bound to {111}$_{NC}$ facets experience an effective attraction resulting in the formation of ligand bridges along the 8-fold $\langle 111 \rangle_{NC}$ directions. This model implies that individual NCs within the NCSL should show both translational and orientational ordering as demonstrated in Figure 5c.

The GIWAXS pattern of the bcc NCSL in Figure 4b shows that this is indeed the case. The wide-angle scattering pattern confirms that the (110)$_{NC}$ orientation of individual NCs is coaxially aligned with the (110)$_{SL}$ orientation of the bcc NCSL. The remarkable degree of orientational and translational ordering is consistent with the NCSL model shown in Figure 5c. Furthermore, the model illustrates how Archimedean cubotahedra, the Wiegner–Seitz cells of the bcc crystal, can pack with complete space filling. The more general relationship between NCSL symmetry and the orientation distribution function of NCs within their lattice sites is summarized in Figure 4c. Comparison of the azimuthal width of the (111)$_{NC}$ reflection in the integrated GIWAXS intensity points to a general trend of decreasing orientational coherence of NCs with increasing the c/a ratio of the superlattice constants. The bcc NCSL ($c/a = 1$) exhibits a relatively narrow angular distribution of the (111)$_{NC}$ reflection (fwhm = 15°). This scattering pattern is consistent with that of a PbS crystal whose (110) direction is parallel to the substrate. The angular breadth of the (111)$_{NC}$ reflection increases along the Bain path as shown in the case of the intermediate bct NCSLs with $c/a = 1.16$ (fwhm = 17°) and 1.31 (fwhm = 24°). Finally, fcc NCSLs
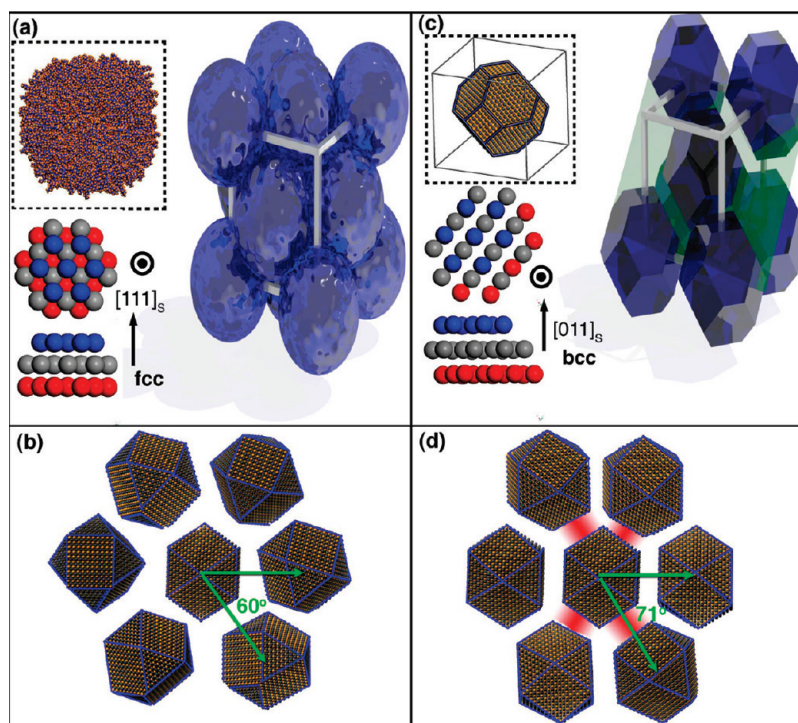
Figure 5. NCSLs with predefined symmetry. Depending on ligand state and solvent content the SL can continuously change from fcc to bcc, with quasi-spherical NCs with extended ligands (fcc), or oriented cuboctahdra (bcc). (a) Model of a fcc superlattice unit cell assembled from quasi-spherical particles. The inset shows a snapshot from a molecular dynamics simulation of the NC-ligand shell complex. The top, right particle is omitted to illustrate the close packing in fcc $(111)_{SL}$ planes. The lower image shows a model of seven PbS NCs in the $(111)_{SL}$ plane of the fcc NCSL. (b) Model of a bcc assembly of cuboctahedral NCs. The green plane indicates the close-packed $(110)_{SL}$ plane of the bcc superlattice. The inset shows a model of a 7 nm PbS nanocrystal with characteristic $(111)_{NC}$ and $(100)_{NC}$ facets of the rock-salt crystal structure. The lower model shows the orientational and translational coherence of NCs in the bcc NCSL. Attractive interactions (in red) between ligands bound to the {111} NC facets drive the orientational coherence of neighboring NCs which in turn drive the change in the NCSL symmetry from fcc to bcc.

showed ringlike WAXS patterns indicative of isotropic distribution of NC orientations within the superlattice sites. These results confirm that the orientational alignment of NCs within their superlattice site provides the impetus for the Bain distortion of the NCSL symmetry.

CONCLUSION

The results presented in this paper demonstrate that solvent vapor processing provides an unprecedented level of control over the assembly of identical NCs into either fcc, bct, or bcc NCSL symmetry (see Figure 5). The NCSL polymorph formation is a well-defined function of deposition kinetics and solvent vapor processing. NCs surrounded by a well-solvated oleic acid ligand shell dispersed in alkane solvent (see MD snapshot in Figure 5a) behave as hard-spheres with short-range attraction and assemble into fcc NCSLs. In the presence of toluene vapor, ligand–ligand

interactions are favored over ligand–solvent interactions; the resulting anisotropic interaction potential reflects the octahedral shape of the NC core leading to the formation of a bcc NCSL with a high degree of orientational and translational order (Figure 5c). NCSLs with bct symmetry and controlled extent of tetragonal distortion can be formed by systematic tuning of the solvent evaporation rate. This high degree of structural control over fcc, bcc, and intermediate bct symmetries along the Bain path opens the door to a rich space of opportunities for the engineering of quantum crystals with desired coherent electrical, magnetic, and optical properties. The formation of such artificial solids from lead salt NCs is particularly intriguing for the investigation of the relationship between the superstructure and coherent properties since the strong quantum and dielectric confinement leads to weak exciton binding and high electronic coupling.

METHODS

Nanocrystal Synthesis. PbSe NCs were prepared following the method reported by Yu et al.[35] The synthesis was carried out in a three-necked flask under an inert nitrogen atmosphere. In a typical synthesis, PbO (4 mmol) and oleic acid (10 mmol) were

dissolved in 1-octadecene (ODE) to yield a precursor solution with [Pb] = 0.3 M and a molar Pb/oleic acid ratio of 1:2.5. The solution was then degassed by heating to 160 °C for 1 h under flowing nitrogen. In a glovebox, Se was dissolved in trioctylphosphine (TOP) to yield a 1 M stock solution. A small amount of

diphenylphospine (DPP) (4.5 mM) was added to the TOPSe solution. A 12 mL portion of the 1 M TOP-Se solution was rapidly injected into the vigorously stirred, hot lead oleate solution. PbSe NCs formed immediately after injection and their size was tuned through adjustments in temperature (120–180 °C), reaction time (0.5–5 min), and molar Pb/oleic acid ratio (1:6 to 1:2). After the elapsed reaction time, the solution was quenched by transferring the flask to a water bath. Following synthesis, the NCs were washed several times by sequential precipitation with ethanol and redispersion in anhydrous hexane. The PbSe NC cores had an average diameter of 6.1 nm with a 11% relative size distribution, based on a statistical analysis of TEM images.

The PbS synthesis was adopted from the work by Hines and Scholes.[36] PbO (1 mmol) and oleic acid (25 mmol) were dissolved in approximately 2 mL of ODE to yield a solution with a total volume of 10 mL. The solution was then degassed by heating to 150 °C for 1 h under flowing nitrogen. In a glovebox, 0.6 mol of bis(trimethylsilyl)sulfide (TMS) was dissolved in 6 mL of ODE and stirred thoroughly. A 5 mL portion of the TMS solution was rapidly injected into the vigorously stirred, hot lead oleate solution. PbS NCs formed immediately after injection, and they were collected after 1 min of reaction at 150 °C. Following synthesis the NCs were washed several times by sequential precipitation with ethanol and redisperson in anhydrous hexane. The PbS NCs had an average diameter of 6.4 nm with a 9% relative size distribution, based on statistical analysis of TEM images.

NC Film Deposition and GISAXS Measurements. NC films were prepared by drop-casting a NC suspension onto a cleaned substrate and drying the film in a controlled vapor environment. Details of the drop-casting deposition are given elsewhere.[24]

Grazing incidence small-angle X-ray scattering (GISAXS) measurements were performed on beamline D1 of the Cornell High Energy Synchrotron Source (CHESS) using monochromatic radiation of wavelength λ = 1.284 Å with a bandwidth $\Delta\lambda/\lambda$ of 1.5%.[37] The X-ray beam was produced by a hardbent dipole magnet of the Cornell storage ring and monochromatized with Mo:B$_4$C synthetic multilayers with a period of 30 Å. The D1 area detector (MedOptics) is a fiber-coupled CCD camera with a pixel size of 46.9 μm by 46.9 μm and a total of 1024×1024 pixels with a 14-bit dynamical range per pixel. Typical read-out time per image was below 5 s. The images were dark current corrected, distortion-corrected, and flat-field corrected by the acquisition software.[38] The sample to detector distance was 938 mm, as determined using a silver behenate powder standard. The incident angle of the X-ray beam was varied between 0.02° and 0.45°; most data presented here were taken at 0.25°, that is, slightly above the silicon critical angle (0.18°). Typical exposure times ranged from 0.1 to 1.0 s. Scattering images were calibrated and integrated using the Fit2D software.[39] GISAXS diffraction peaks were indexed and fitted using our in-house software.[40] WAXS patterns were recorded on an imaging plate and scanned for digital processing. Details of the solvent vapor chamber used for *in situ* GISAXS measurement setup are provided in the Supporting Information.

Molecular Dynamics Simulations. Models for the "capping" ligands, oleic acid and C$_{11}$H$_{23}$COOH (the so-called "C12" ligand), were created using the Molden software package,[41] and an energy minimization of the initial guessed structures was performed using a standard minimization algorithm, here the limited memory L-BFGS minimization using a modified version of the Nocedal algorithm, which is a part of the TINKER software package.[42] The length of the oleic acid ligand was measured to be 1.8 nm and the "C12" ligand was measured to be 1.4 nm; knowledge of these lengths are needed in order to estimate the extent of interpenetration of the ligands on adjacent nanocrystals.

Intermolecular Potential Model. The only input, beyond processing conditions, to the deterministic Molecular Dynamics technique is the intermolecular potential model. We chose to use the nonreactive semiempirical MM3 potential to model all the ligand interactions. There are no crystal core–core interactions to consider here because we assumed, based on the prior work of Luedtke and Landman,[29] that the ligand–ligand interactions dominate over the NC–NC ones in the absence of long-range

dipole–dipole interactions, which is the case here. The MM3 potential has been shown, by us and others, to accurately describe aliphatic hydrocarbons and three-, four-, five-, and six-ringed organic structures. MM3 incorporates stretching, bending, and torsional energies, as well as the van der Waals interaction energies based on phenomenologically determined parameters. We have used this model extensively and successfully to study the energetics and structural characteristics of an array of small organic molecules including the acenes, rubrene, DIP, sexiphenyl, and C$_{60}$. Our most recent study involved an extensive survey of 12 Density Functional Theory models, as well as the MM3 and MM3-π models for the sexiphenyl molecule, in which we found all 14 models to give consistent energetically preferred structures.[43] Detailed aspects of the MD simulations are provided in section 8 of the Supporting Information.

Supporting Information Available: Statistical analysis of NC dipole distribution, *in situ* GISAXS measurement setup, particle concentration of NC suspensions, NCSL grain size analysis, relationship between colloidal concentration, growth rate, and superlattice symmetry, transmission and scanning electron microscopy images, infrared spectroscopy, and details of MD simulations. This material is available free of charge *via* the Internet at http://pubs.acs.org.

REFERENCES AND NOTES

1. Korgel, B.; Fitzmaurice, D. Small-Angle X-ray-Scattering Study of Silver-Nanocrystal Disorder–Order Phase Transitions. *Phys. Rev. B: Condens. Matter Mater. Phys.* **1999,** *59*, 14191–14201.

2. Whetten, R. L.; Shafigullin, M. N.; Khoury, J. T.; Schaaff, T. G.; Vezmar, I.; Alvarez, M. M.; Wilkinson, A. Crystal Structures of Molecular Gold Nanocrystal Arrays. *Acc. Chem. Res.* **1999,** *32*, 397–406.

3. Bain, E. The Nature of Martensite. *Trans. Am. Inst. Miner. Metall. Eng.* **1924,** *70*, 25–46.

4. Bang, J.; Lodge, T. Mechanisms and Epitaxial Relationships between Close-Packed and BCC Lattices in Block Copolymer Solutions. *J. Phys. Chem. B* **2003,** *107*, 12071–12081.

5. Buschbeck, J.; Opahle, I.; Richter, M.; Roessler, U. K.; Klaer, P.; Kallmayer, M.; Elmers, H. J.; Jakob, G.; Schultz, L.; Faehler, S. Full Tunability of Strain along the fcc–bcc Bain Path in Epitaxial Films and Consequences for Magnetic Properties. *Phys. Rev. Lett.* **2009,** *103*, 216101.

6. Jona, F.; Marcus, P. Structural Properties of Copper. *Phys. Rev. B: Condens. Matter Mater. Phys.* **2001,** *63*, 094113.

7. Ma, H.; Qiu, S.; Marcus, P. Pressure Instability of bcc Iron. *Phys. Rev. B: Condens. Matter Mater. Phys.* **2002,** *66*, 024113.

8. Mikhaylushkin, A. S.; Abrikosov, I. A.; Belonoshko, A. B.; Johansson, B.; Simak, S. I. Instability of the Body-Centered Tetragonal Phase of Iron Under Extreme Conditions. *Phys. Rev. B: Condens. Matter Mater. Phys.* **2009,** *79*, 132106.

9. Bishop, K. J. M.; Wilmer, C. E.; Soh, S.; Grzybowski, B. A. Nanoscale Forces and Their Uses in Self-Assembly. *Small* **2009,** *5*, 1600–1630.

10. Burgers, W. On the Process of Transition of the Cubic-Body-Centered Modification into the Hexagonal-Close-Packed Modification of Zirconium. *Physica* **1934,** *1*, 561–586.

11. Opahle, I.; Koepernik, K.; Nitzsche, U.; Richter, M. Jahn—Teller-like Origin of the Tetragonal Distortion in Disordered Fe—Pd Magnetic Shape Memory Alloys. *Appl. Phys. Lett.* **2009,** *94,* 072508.

12. Wentzcovitch, R. M.; Krakauer, H. Martensitic Transformation of Ca. *Phys. Rev. B: Condens. Matter Mater. Phys.* **1990,** *42,* 4563–4567.

13. Trinkle, D. R.; Hennig, R. G.; Srinivasan, S. G.; Hatch, D. M.; Jones, M. D.; Stokes, H. T.; Albers, R. C.; Wilkins, J. W. New Mechanism for the Alpha to Omega Martensitic Transformation in Pure Titanium. *Phys. Rev. Lett.* **2003,** *91,* 025701.

14. Cho, K.-S.; Talapin, D. V.; Gaschler, W.; Murray, C. B. Designing PbSe Nanowires and Nanorings through Oriented Attachment of Nanoparticles. *J. Am. Chem. Soc.* **2005,** *127,* 7140–7147.

15. Shim, M.; Guyot-Sionnest, P. Permanent Dipole Moment and Charges in Colloidal Semiconductor Quantum Dots. *J. Chem. Phys.* **1999,** *111,* 6955–6964.

16. Klokkenburg, M.; Houtepen, A. J.; Koole, R.; de Folter, J. W. J.; Erne, B. H.; van Faassen, E.; Vanmaekelbergh, D. Dipolar Structures in Colloidal Dispersions of PbSe and CdSe Quantum Dots. *Nano Lett.* **2007,** *7,* 2931–2936.

17. Hanrath, T.; Veldman, D.; Choi, J. J.; Christova, C. G.; Wienk, M. M.; Janssen, R. A. J. PbSe Nanocrystal Network Formation During Pyridine Ligand Displacement. *ACS Appl. Mater. Interfaces* **2009,** *1,* 244–250.

18. Talapin, D. V.; Shevchenko, E. V.; Murray, C. B.; Titov, A. V.; Kral, P. Dipole—Dipole Interactions in Nanoparticle Superlattices. *Nano Lett.* **2007,** *7,* 1213–1219.

19. Fang, C.; van Huis, M. A.; Vanmaekelbergh, D.; Zandbergen, H. W. Energetics of Polar and Nonpolar Facets of PbSe Nanocrystals from Theory and Experiment. *ACS Nano* **2010,** *4,* 211–218.

20. Luther, J. M.; Law, M.; Song, Q.; Perkins, C. L.; Beard, M. C.; Nozik, A. J. Structural, Optical, and Electrical Properties of Self-Assembled Films of PbSe Nanocrystals Treated with 1,2-Ethanedithiol. *ACS Nano* **2008,** *2,* 271–280.

21. Moreels, I.; Fritzinger, B.; Martins, J.; Hens, Z. Surface Chemistry of Colloidal PbSe Nanocrystals. *J. Am. Chem. Soc.* **2008,** *130,* 15081–15086.

22. Talapin, D. V.; Murray, C. B. PbSe Nanocrystal Solids for n- and p-Channel Thin Film Field-Effect Transistors. *Science* **2005,** *310,* 86–89.

23. Hanrath, T.; Choi, J. J.; Smilgies, D. Structure/Processing Relationships of Highly Ordered Lead Salt Nanocrystal Superlattices. *ACS Nano* **2009,** *3,* 2975–2988.

24. Scherrer, P. Bestimmung der Grösse und der inneren Struktur von Kolloidteilchen mittels Röntgenstrahlen. *Nachr. Ges. Wiss. Göttingen* **1918,** *26,* 98–100.

25. Gemici, Z.; Schwachulla, P. I.; Williamson, E. H.; Rubner, M. F.; Cohen, R. E. Targeted Functionalization of Nanoparticle Thin Films *via* Capillary Condensation. *Nano Lett.* **2009,** *9,* 1064–1070.

26. Alexander, S.; McTague, J. Should All Crystals be bcc? Landau Theory of Solidification and Crystal Nucleation. *Phys. Rev. Lett.* **1978,** *41,* 702–705.

27. Choi, J. J.; Bealing, C. R.; Bian, K.; Hughes, K. J.; Zhang, W.; Smilgies, D.-M.; Hennig, R. G.; Engstrom, J. R.; Hanrath, T. Controlling Nanocrystal Superlattice Symmetry and Shape-Anisotropic Interactions Through Variable Ligand Surface Coverage. *J. Am. Chem. Soc.* **2011**, ASAP, DOI: 10.1021/ja110454b.

28. Luedtke, W.; Landman, U. Structure and Thermodynamics of Self-Assembled Monolayers on Gold Nanocrystallites. *J. Phys. Chem. B* **1998,** *102,* 6566–6572.

29. Luedtke, W. D.; Landman, U. Structure, Dynamics, and Thermodynamics of Passivated Gold Nanocrystallites and Their Assemblies. *J. Phys. Chem.* **1996,** *100,* 13323–13329.

30. Li, Y. Y.; Lin, S. T.; Goddard, W. A. Efficiency of Various Lattices From Hard Ball to Soft Ball: Theoretical Study of Thermodynamic Properties of Dendrimer Liquid Crystal from Atomistic Simulation. *J. Am. Chem. Soc.* **2004,** *126,* 1872–1885.

31. Badia, A.; Singh, S.; Demers, L.; Cuccia, L.; Brown, G.; Lennox, R. Self-Assembled Monolayers on Gold Nanoparticles. *Chem.—Eur. J.* **1996,** *2,* 359–363.

32. Henry, A.-I.; Courty, A.; Pileni, M.-P.; Albouy, P.-A.; Israelachvili, J. Tuning of Solid Phase in Supracrystals Made of Silver Nanocrystals. *Nano Lett.* **2008,** *8,* 2000–2005.

33. Wang, Z.; Harfenist, S.; Whetten, R.; Bentley, J.; Evans, N. Bundling and Interdigitation of Adsorbed Thiolate Groups in Self-Assembled Nanocrystal Superlattices. *J. Phys. Chem. B* **1998,** *102,* 3068–3072.

34. Chen, Z.; Moore, J.; Radtke, G.; Sirringhaus, H.; O'Brien, S. Binary Nanoparticle Superlattices in the Semiconductor—Semiconductor System: CdTe and CdSe. *J. Am. Chem. Soc.* **2007,** *129,* 15702–15709.

35. Yu, W. W.; Falkner, J. C.; Shih, B. S.; Colvin, V. L. Preparation and Characterization of Monodisperse PbSe Semiconductor Nanocrystals in a Noncoordinating Solvent. *Chem. Mater.* **2004,** *16,* 3318–3322.

36. Hines, M. A.; Scholes, G. D. Colloidal PbS Nanocrystals with Size-Tunable Near-Infrared Emission: Observation of Post-Synthesis Self-Narrowing of the Particle Size Distribution. *Adv. Mater. (Weinheim, Ger.)* **2003,** *15,* 1844–1849.

37. Smilgies, D.-M.; Busch, P.; Posselt, D.; Papadakis, C. M. Characterization of Polymer Thin Films with Small-Angle X-ray Scattering under Grazing Incidence (GISAXS). *Synchrotron Radiat. News* **2002,** *15,* 35–41.

38. Gruner, S. M.; Tate, M. W.; Eikenberry, E. F. Charge-Coupled Device Area X-ray Detectors. *Rev. Sci. Instrum.* **2002,** *73,* 2815–2842.

39. Hammersley, A. P. *ESRF Internal Report, ESRF97HA02T "FIT2D: An Introduction and Overview"*; ESRF:Grenoble, France,1997.

40. Smilgies, D. M.; Blasini, D. R. Indexation Scheme for Oriented Molecular Thin Films Studied with Grazing-Incidence Reciprocal-Space Mapping. *J. Appl. Crystallogr.* **2007,** *40,* 716–718.

41. Schaftenaar, G.; Noordik, J. H.; Molden: A Pre- and Post-processing Program for Molecular and Electronic Structures. *J. Comput.-Aided Mol. Des. 14,* 123-134.

42. TINKER: Software Tools for Molecular Design ; http://dasher.wustl.edu/tinker/, 2010.

43. Goose, J. E.; First, E.; Clancy, P. Nature of Step-Edge Barriers for Small Organic Molecules. *Phys. Rev. B: Condens. Matter Mater. Phys.* **2010,** *81,* 205310.